designs

MDPI

Article

Dynamic Analysis of Transmission Wire Impact on Hanging Net Shielding System

Qiang Liu [1], Xi Zheng [1], Qiuhan Zhang [1], Yongjian Bian [2] and Zuqing Yu [2,*]

[1] Xuzhou Power Transmission & Transformation Co., Ltd., Xuzhou 221000, China
[2] College of Mechanical and Electrical Engineering, Hohai University, Changzhou 213022, China
* Correspondence: yuzq@hhu.edu.cn

Abstract

The hanging net shielding system, employing a suspended cage-type enclosed structure to restrict the high-voltage transmission wire, has seen increasingly widespread application in transmission line crossing construction. However, the lack of a comprehensive dynamic analysis methodology has limited the standardization of its design and usage. In this investigation, a systematical dynamic modeling and analysis procedure of the hanging net shielding system is proposed based on the absolute nodal coordinate formulation (ANCF). The carrier cable, slings and transmission wire are discretized by the ANCF cable element. The spatial flexible beam–beam contact model and the assumption of a single contact area are adopted to perform the contact searching between the transmission wire and the horizontal pulley. The system dynamics analysis equation is assembled and solved by generalized alpha method. A full-scale model is simulated for the transmission wire impact condition and the variation history of the tension in carrier cable and the sling cable are given. The peak value of the tension in carrier cable could be 110 kN, while the largest tension in sling cable is 9 kN. Results could help to ensure construction safety, shorten the design cycle of the protection system and reduce the development cost at the same time.

Keywords: transmission wire; crossing construction; hanging net; absolute node coordinate formulation; multibody system dynamics

1. Introduction

During the crossing construction process of power transmission line construction, conductors will inevitably cross existing facilities such as expressways, railways and buildings. If a wire breaks, it will impact the existing facilities below with tremendous kinetic energy. Therefore, protective devices need to be installed to withstand the impact of the conductors. At present, there is no unified plan or engineering design standard for such protective facilities in the industry. At present, a shielding system with a hanging net structure, which is shown in Figure 1, has been widely applied in engineering, but its impact resistance mechanical performance has not yet been theoretically verified. The difficulty lies in the fact that the impact load is influenced by multiple factors, and the wires and flexible ropes have a geometric nonlinear behavior of large-scale motion and deformation coupling, which makes it difficult to obtain their dynamic responses.

Check for updates

Academic Editors: Marco Carnevale and Pedro Aires Montenegro

Received: 4 December 2025
Revised: 23 January 2026
Accepted: 10 February 2026
Published: 17 February 2026

Copyright: © 2026 by the authors. Licensee MDPI, Basel, Switzerland. This article is an open access article distributed under the terms and conditions of the Creative Commons Attribution (CC BY) license.

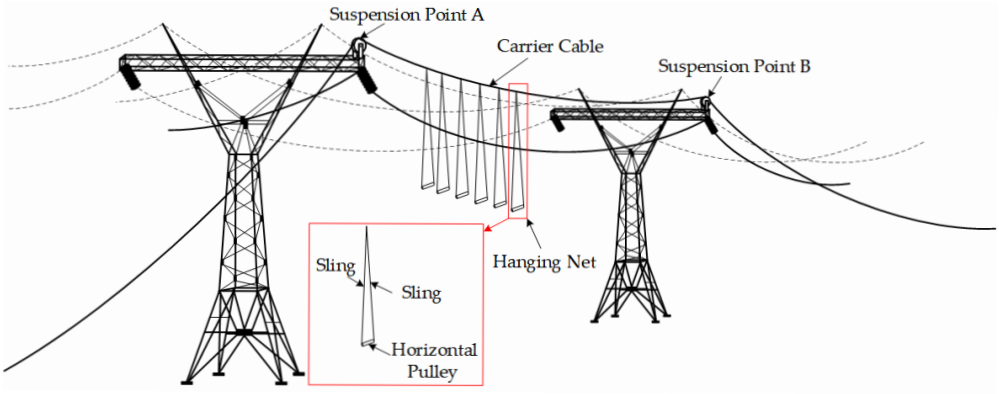


Figure 1. Hanging net shielding system.

Existing research often focuses on the dynamic characteristics and behavior of transmission line conductors themselves. In the research proposed by Barbieri et al., the dynamical modeling analysis of the transmission line cables and its damping estimation were given [1,2]. Another important research direction is the prediction of the galloping behavior of wires under conditions of ice coverage or severe wind loads [3]. When extreme weather conditions such as freezing rain occur, the shape of the ice layer covering the surface of the conductors will change their response characteristics in the wind field, thereby intensifying the galloping behavior and eventually leading to line collapse accidents [4,5]. Gao et al. [6] studied the galloping characteristics of ice-coated transmission lines under oblique flows based on wind tunnel tests. Zhao et al. [7] built a real transmission tower line system test platform and studied the vibration characteristics of iced conductors with and without D-shaped cross-sections. They found that the vibration of iced conductors is mainly in their low order modes. Qin et al. [8] conducted a study on a large-span transverse rope suspension system with suspension insulators, using theoretical modeling methods and finite element analysis. The displacement of suspension insulators increases with the increase in wind speed, but the number of spans has little effect on tension and deformation. Sørum et al. [9] investigated the effectiveness of modeling polyester mooring lines using bi-linear and Syrop stiffness models. The bi-linear model artificially reduces the tension range, especially when there is a significant difference between the quasi-static stiffness and dynamic stiffness of the fiber rope. The Syrop model considers quasi-static and permanent rope elongation, while analyzing with dynamic stiffness. Hong et al. [10] established a dynamic model of high-speed elevator traction wire rope and conducted numerical simulation analysis on the motion process. Kang et al. [11] designed a new calculation method to determine the dynamic stiffness of polyester ropes and studied the dynamic performance of polyester ropes. Cheng et al. [12] analyzed the dynamic response of transmission line tower systems under fluctuating wind. In order to improve computational efficiency, an efficient computational model was developed based on the free interface modal synthesis method. High computational efficiency is achieved while ensuring high precision. Prakash et al. [13] developed a comprehensive model to study the reliability of transmission lines, which focuses on analyzing faults in transmission lines, mainly considering the effects of wind, environmental temperature, and current demand, including minimal and significant pre-existing damage. Deng et al. [14] studied the stress/strain characteristics at the root of the wire rope joints under axial impact and tensile bending combined loads and determined the failure location and quantified the relative stress magnitude under complex loads.

From the summary above, one can find that research on safety protection technologies and equipment during the construction process of transmission line crossing is less common in the literature. In a paper published by Gu et al. [15], the authors established a dynamic modeling and analysis algorithm for large-scale lattice crossing frame structures after a

wire breakage accident. Subsequently, in 2025, the author proposed a flexible nylon rope net structure for crossing protection systems and provided an efficient modeling and solution strategy for such protection systems due to wire breakage impacts [16]. Xia et al. [17] established a multi-body system model for flexible protection in transmission engineering in 2025. The accuracy of the proposed model was verified through numerical simulation and experimental comparison.

Through the research and analysis of existing literature, the author believes that there is relatively little research work on the protection technology and equipment for transmission line crossing construction. This is mainly due to the fact that there are various types of protective equipment for crossing construction, and their working principles are also different. In addition, such problems often involve complex dynamic behaviors such as large deformation of flexible bodies and collision impacts, making modeling and analysis rather difficult. On the other hand, absolute nodal coordinate formulation (ANCF) is suitable for the description of the flexible body dynamics, especially for large rotation and deformations. After years of development, this theory now has a complete unit library, and some units have also been tested in engineering practice [18]. The ANCF cable element, which was proposed by Gerstmayr and Irschik, was validated through large deformation numerical examples [19]. In the research work proposed by Wang et al., the cable element was utilized to capture the dynamic response when two thin beams came into contact. The contact force was composed within multiple continuous contact zones [20,21]. In the field of high-speed railways, ANCF cable element was used to establish transmission line modeling and pantograph/catenary interactions [22,23]. In the research work reported by Peng et al., an adaptive length-varying ANCF cable element was proposed to depict the initial equilibrium configuration of railway catenaries [24]. In the field of aerospace engineering, ANCF cable units are used in the pre-research and feasibility study of space elevator projects [25]. Based on ANCF cable element, Takayama et al. proposed a systematical modeling and calculation procedure to simulate the contact between the inlet and the tether, with the slit shape being taken into consideration [26]. Afterwards, they conducted a detailed study on the influence of slit shape on the control responsiveness during the extension and winding process of the tether. Yue et al. carried out a strain-decoupled ANCF cable element, obtaining an equivalent [27]. Zhang et al. improved the calculation efficiency of ANCF cable element elastic by giving a new dot product form of curvature [28]. The arbitrary Lagrangian–Eulerian (ALE) ANCF cable element was utilized by Wang et al. to study the traverse obstacles of the underwater tethered systems with varying lengths [29]. By modifying the manner of torque transmission at sheaves, Escalona et al. introduced a new modeling method based on ALE-ANCF elements to simulate the dynamics of reeving systems [30]. In the field of construction machinery, steel wire ropes, as a kind of flexible component with large deformation, are often the difficulty in dynamic modeling and analysis. In the research published by Li et al., the ALE-ANCF cable element was used to describe the wire rope with length variations in the hoisting mechanism of tower cranes, and a command smoothing algorithm that can be used to suppress the swing after the load is positioned was presented [31]. Han et al. [32] developed a detailed contact dynamics model of the rope-sheave system, based on ANCF. This model can be used to improve the motion control strategy of traction systems and reduce energy loss.

In summary, the existing research on the dynamic analysis of safety protection technology for suspended grid construction during transmission line crossing construction is insufficient. The research on the design theory and dynamic analysis of crossing construction protection devices mostly employs commercial finite element software for modeling and analysis. Particularly, research on crossing protection devices in the hanging net shielding system remains unexplored. It is the aim of this investigation that establishing a flexible

multibody system model for the transmission line and hanging net shielding system. To this end, the ANCF will be employed as theoretical foundation and the cable element will be used as discretization tool. The key modeling issues will be discussed. Firstly, the initial configuration of the carrier cable is calculated based on the catenary formula, with the horizontal and vertical distances between the suspension points at both ends of the carrier cable, as well as the tension force, as the input variables. From this, the initial values of the nodal position and gradient vectors of the ANCF finite element mesh can be obtained. Secondly, the contact searching algorithm between the wire and the horizontal pulley is designed to find the boundary of contact zone, over which the contact force is integrated. Finally, the system equation of motion is assembled and solved. Accordingly, the dynamic process of the transmission wire impacting the shielding system can be depicted. The value and location of the largest tension within the system can be obtained. This will shorten the design cycle of the protection system and reduce the development cost.

2. Kinetic Description

2.1. Absolute Nodal Coordinate Formulation

This study employs the ANCF cable element based on the Euler–Bernoulli beam hypothesis to model the wire rope. As shown in Figure 2, the element utilizes the global position vectors and the gradient vectors along the axial direction at the first and last nodes as nodal coordinates, resulting in a total of 12 degrees of freedom. The global coordinate of any point on the central axis of the element is given by $\mathbf{r} = \mathbf{Se}$, where $\mathbf{e}$ is the vector of element nodal coordinates, and $\mathbf{S}$ is the shape function matrix:

$$\mathbf{S} = [S_1\mathbf{I}_{3\times3}, S_2\mathbf{I}_{3\times3}, S_3\mathbf{I}_{3\times3}, S_4\mathbf{I}_{3\times3}] \tag{1}$$

In the equation above, $\mathbf{I}_{3\times3}$ is the 3-by-3 identity matrix. The components of the shape function matrix are:

$$S_1 = 1 - 3\xi^2 + 2\xi^3, S_2 = l\left(\xi - 2\xi^2 + \xi^3\right), S_3 = 3\xi^2 + 2\xi^3, S_4 = l\left(-\xi^2 + \xi^3\right) \tag{2}$$

where $\xi = x/l$ is the non-dimensional material coordinate characterizing any point within the element, x is the material coordinate, and l is the length of the element in its initial configuration. The element mass matrix, which has the unit of kg, has the following expression:

$$\mathbf{M}^{\mathrm{e}} = \int_V \rho \mathbf{S}^{\mathrm{T}}\mathbf{S}\mathrm{d}V \tag{3}$$

where ρ and V are the density and volume of the element.

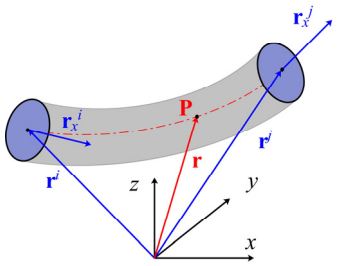


Figure 2. ANCF cable element.

It is evident that the expression for the element mass matrix does not contain nodal coordinates and is thus independent of the current configuration. This implies that the mass matrix is constant, which is one of the most significant advantages of the ANCF. This property allows for the computation and decomposition of the flexible body mass matrix

in the pre-processing stage of a computer implementation, thereby reducing computational load and improving efficiency during the solution of the dynamic equations.

2.2. Elastic Force Model

Due to the adoption of the Euler–Bernoulli beam hypothesis, which neglects cross-sectional compression and shear, the general expressions of continuum mechanics are not directly applicable to the cable element. The element elastic energy is based on the geometric description of a spatial curve, comprising axial stretching and bending components. Consequently, the integral changes from volume integral to line integral along the central axis:

$$U = \frac{1}{2}\int_0^l EA(\varepsilon_{xx})^2 \mathrm{d}x + \frac{1}{2}\int_0^l EI(\kappa)^2 \mathrm{d}x \tag{4}$$

where U (J) is the elastic energy, E is Young's modulus, A and I are the cross-sectional area and the second moment of area (moment of inertia) of the element, respectively. $\varepsilon_{xx} = |\mathbf{r}_x| - 1$ is the axial strain of the element, and $\kappa = |\mathbf{r}_x \times \mathbf{r}_{xx}|/|\mathbf{r}_x|^2$ is the curvature of the central axis. $\mathbf{r}_x$ and $\mathbf{r}_{xx}$ are the first- and second-order gradient vectors with respect to the axial direction, respectively. The generalized elastic force of the element is obtained by taking the partial derivative of the elastic energy with respect to the element nodal coordinates:

$$\mathbf{Q}_\mathrm{e} = \frac{\partial U}{\partial \mathbf{e}} = \mathbf{Q}_\mathrm{s} + \mathbf{Q}_\kappa \tag{5}$$

where $\mathbf{Q}_\mathrm{s}$ and $\mathbf{Q}_\kappa$ are the generalized elastic forces related to axial stretching and bending, respectively. Their units are newtons, and their expressions are:

$$\mathbf{Q}_\mathrm{s} = \int_0^l EA\varepsilon_{xx}\frac{\partial \varepsilon_{xx}}{\partial \mathbf{e}}\mathrm{d}x,\ \mathbf{Q}_\kappa = \int_0^l EI\kappa\frac{\partial \kappa}{\partial \mathbf{e}}\mathrm{d}x \tag{6}$$

In the above equations, both axial strain and curvature are scalars, their derivatives with respect to the nodal coordinate vector yield vectors of the same dimension. The definitions of their components are respectively:

$$\begin{aligned}\frac{\partial \varepsilon_{xx}}{\partial e_i} &= \frac{\partial(|\mathbf{r}_x|-1)}{\partial e_i} = \frac{\partial |\mathbf{r}_x|}{\partial e_i} = \frac{\partial \left(\mathbf{r}_x^T\mathbf{r}_x\right)^{\frac{1}{2}}}{\partial e_i} = \frac{1}{2}\left(\mathbf{r}_x^T\mathbf{r}_x\right)^{-\frac{1}{2}}\frac{\partial\left(\mathbf{r}_x^T\mathbf{r}_x\right)}{\partial e_i} \\ &= \frac{1}{2}\frac{1}{|\mathbf{r}_x|}\left(\mathbf{S}_{x,i}^\mathrm{T}\cdot\mathbf{r}_x + \mathbf{r}_{x,i}^\mathrm{T}\cdot\mathbf{S}_x\right) = \frac{1}{|\mathbf{r}_x|}\left(\mathbf{S}_{x,i}^\mathrm{T}\cdot\mathbf{r}_x\right)\end{aligned} \tag{7}$$

where e_i is the i-th component of the nodal coordinate vector, and $\mathbf{S}_{x,i}$ is the i-th column of the matrix $\mathbf{S}_x$, the derivative of the element shape function with respect to the material coordinate. To facilitate the derivation of the curvature derivative expression, define $f = |\mathbf{r}_x \times \mathbf{r}_{xx}|$ and $g = |\mathbf{r}_x|^2$. The derivative of the curvature κ with respect to the i-th nodal coordinate component is then given by the expression:

$$\frac{\partial \kappa}{\partial e_i} = \frac{\partial}{\partial e_i}\left(\frac{f}{g}\right) = \frac{1}{g^2}\left(\frac{\partial f}{\partial e_i}g - f\frac{\partial g}{\partial e_i}\right) \tag{8}$$

The derivatives of the numerator f and the denominator g are:

$$\frac{\partial f}{\partial e_i} = \frac{1}{f}(\mathbf{S}_{x,i}\times\mathbf{r}_{xx} + \mathbf{r}_x\times\mathbf{S}_{xx,i})^\mathrm{T}\cdot(\mathbf{r}_x\times\mathbf{r}_{xx}),\ \frac{\partial g}{\partial e_i} = 2\cdot\mathbf{S}_{x,i}^\mathrm{T}\cdot\mathbf{r}_x \tag{9}$$

where $\mathbf{S}_{xx,i}$ is the i-th column of the matrix $\mathbf{S}_{xx}$, the second derivative of the element shape function with respect to the material coordinate. It should be noted that if an implicit integrator is used to solve the system equation of motion, the Jacobian matrix of the elastic force with respect to the element nodal coordinate vector will be required. Following the

same manner given in this section, one can find the formulation. This is omitted here due to space constraints.

2.3. Initial Configuration of the Carrier Cable

In the design of the hanging net shielding system, the carrier cable serves as the primary load-bearing component. The determination of its initial tension and sag directly influences the system's geometric stability under unloaded conditions, its dynamic response during operation, and the safety clearance to obstacles. In practical engineering applications, the horizontal and vertical differences between two suspension points, along with the initial tension, are three key parameters that affect the initial configuration of the carrier cable. Among them, the horizontal and vertical distances between the suspension points are usually the boundary conditions for construction, while the initial tension is adjusted by on-site technicians through tensioning machines. In engineering, catenary lines are usually adopted as hypothetical curves to describe the configuration of the carrier cable, as illustrated in Figure 3. It means that through force analysis based on the assumption of the catenary curve, the relationship between the initial tension and the magnitude of the sag can be obtained.

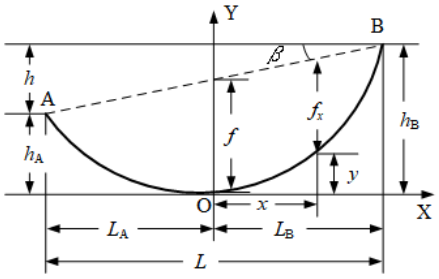


Figure 3. Catenary curve of the carrier cable.

In Figure 3, A and B are the two suspension points. They are the contact point of the carrier cable with the pulleys on the iron tower at two sides of the crossing object, which is also shown in Figure 1. When the locations of two suspension points are determined, establishing the coordinate system as shown in Figure 3, one can obtain the formulation for the initial configuration of the carrier cable through the industry standard [33]:

$$fx = \frac{T}{w}\left(\cosh\left(\frac{wL}{2T}\right) - \cosh\left(\frac{w}{T}x\right)\right) - \frac{\mathrm{sgn}(h)\cdot h}{L}(L_A + x) \tag{10}$$

where f_x (m) is the arc sag value at an arbitrary point on the cable which is specified by x coordinate. T is the composed initial tension on the carrier cable, and w is the linear density. L and h are the horizontal and vertical distance between the suspension points A and B, respectively. L_A is the horizontal distance between the left suspension point and point O, which is the lowest point of the arc. The definition of other variables could be found in Figure 3. Through this equation, configuration of the entire carrier cable can be obtained. In other words, the position and gradient vectors which are required by ANCF nodes can be provided. The discretization based on ANCF cable element can be performed.

3. Contact Simulation

Accurate detection and simulation of the contact between the wire and the horizontal pulley is a key challenge in the dynamic analysis of the impacting process. In this investigation, three basic assumptions are made. First, the wire, which is discretized by ANCF cable elements, can be seen as a spatial curve. The contact detection is performed between each horizontal pulley and the entire wire. Second, a single and continuous contact zone will be formed between the wire and each horizontal pulley in contact. In fact, some studies

have hypothesized that the contact between spatial flexible beams happens on multi-zones. However, this assumption is more applicable when both beams have relatively high flexibility, and the winding length is very large. In this study, the deformation of the horizontal pulley is relatively small, so the assumption of single-zone contact is sufficient to meet the requirements [20,21]. Third, the contact force is defined as a distributed force within the contact zone through penalty method, which is widely used in contact simulation for its simplicity, no introduction of additional equations and easy interpretation from a viewpoint of physics [21]. Of course, the penalty method has limitations, such as parameter sensitivity and complexity in the implicit solution format. As shown in Figure 4, the common normal between the wire element and the pulley is found by using a bivariate Newton iteration to obtain the minimum distance between the wire and horizontal pulley. If the minimum distance is greater than the sum of the radii of the wire and the pulley, the contact searching algorithm will move on to the next horizontal pulley.

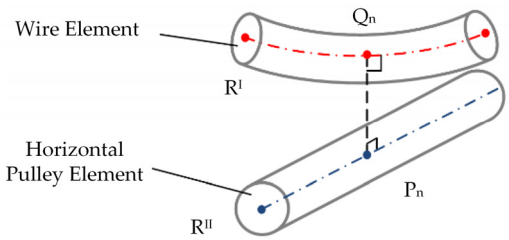


Figure 4. State of non-contact between wire element and horizontal pulley element.

If the previous step detects that the minimum distance between the wire and the pulley is less than the sum of their radii, it is indicated that the contact occurs. Next, the contact searching algorithm will start from the vertical foot to find the boundary of the contact zone by using the bisection method. Consequently, the interval of the material coordinates corresponding to the contact zone on the wire and the horizontal pulley can be obtained respectively, which are [$\mathbf{Q}_a$, $\mathbf{Q}_b$] on the wire, and [$\mathbf{P}_a$, $\mathbf{P}_b$] on the pulley, as shown in Figure 5. Subsequently, several Gauss points are distributed within the contact zone. The normal vector $\mathbf{V}_n$, the tangential vector $\mathbf{V}_t$, the penetration depth δ, and the penetration velocity $\dot{\delta}$ are calculated at each Gauss point.

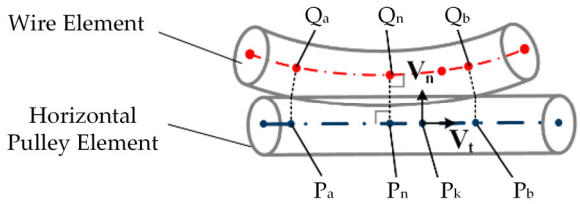


Figure 5. State of contact between wire element and horizontal pulley element.

The contact force at this Gauss point is then calculated using the penalty method:

$$\begin{cases} \mathbf{f} = f_{\mathrm{n}}\mathbf{V}_{\mathrm{n}} + f_{\mathrm{t}}\mathbf{V}_{\mathrm{t}} \\ f_{\mathrm{n}} = k\delta + c|\delta|\dot{\delta},\ f_{\mathrm{t}} = \mu f_{\mathrm{n}} \end{cases} \tag{11}$$

where f_{n} and f_{t} are the amplitude of the normal and tangential contact force respectively. $k = 3800$ N/m is the contact stiffness coefficient, $c = 5$ N·s/m is the contact damping coefficient, and $\mu = 0.13$ is the dynamic friction coefficient. The selection of these parameters is mainly based on the recommendations of the Adams 2024 software and the empirical feedback provided by the actual simulation results. Finally, integrating the contact force

calculated by the equation over the entire contact area yields the generalized contact force $\mathbf{Q}$c of the wire on the pulley:

$$\mathbf{Q}_c = \sum_{k=1}^{n_c} w_k \mathbf{S}_k^T \mathbf{f} \tag{12}$$

where n_c is the number of Gauss points in the contact region, w_k is the Gauss integration weight coefficient, and $\mathbf{S}_k$ is the shape function of the cable element currently in contact.

4. System Assembly and Dynamics Equation Establishment

As mentioned earlier, the wire and the shielding system are uniformly discretized using ANCF cable elements to establish the equations of motion. The connection between components can be conveniently achieved through linear constraints, thereby enabling the description of the entire system with a single mesh. As shown in Figure 6, the net is composed of two slings and a horizontal pulley, suspended from the carrier cable. Therefore, for a single hanging-net, the following kinematic constraints exist:

$$\mathbf{r}^{P_1} = \mathbf{r}^{P_2},\ \mathbf{r}^{P_1} = \mathbf{r}^{P_3},\ \mathbf{r}^{Q_1} = \mathbf{r}^{Q_2},\ \mathbf{r}^{R_1} = \mathbf{r}^{R_2} \tag{13}$$

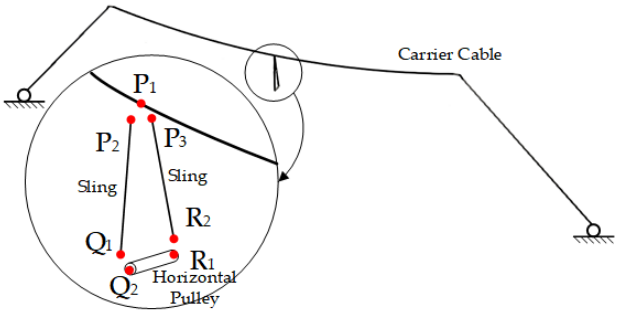


Figure 6. Assembly of the hanging-net and carrier cable.

In the equation above, the variable represents the global position vector of the point denoted by its superscript. Equation (13) provides four vector equations, representing 12 scalar equations. They are typical linear constraints since the Jacobian matrix is constant, which means they can be used to identify and eliminate dependent coordinates from the system generalized coordinates at the preprocessing stage. However, this also means that at each time step, all node coordinates need to be restored using the velocity transformation matrix, leading to low calculation efficiency in the large-scale problems. Therefore, it is recommended to use the first kind of Lagrange equations to obtain the system equation of motion as follows:

$$\begin{cases} \mathbf{M}\ddot{\mathbf{e}} + \mathbf{C}_\mathbf{e}^\mathrm{T}\boldsymbol{\lambda} + \mathbf{Q}_e - \mathbf{Q}_c = 0 \\ \mathbf{C}(\mathbf{e}, t) = 0 \end{cases} \tag{14}$$

In Equation (14), $\mathbf{M}$ is the system mass matrix, $\mathbf{C}$ represents the constraint equations, including linear and nonlinear ones. $\mathbf{C}_\mathbf{e}$ is the Jacobian matrix of the constraints. $\mathbf{Q}_c$ is the generalized contact force, which is defined in Section 3. Equation (14) are typical Index-3 differential-algebraic equations, which can be solved by various integrators. In this investigation, the generalized alpha method is chosen so as to achieve an optimal combination of accuracy, efficiency and robustness in tough problems.

5. Simulation and Analysis

In order to verify the modeling and analysis method proposed in this paper, a real scale model of the hanging net shielding system, as shown in Figure 7, is established. The span distance is 150 m. The carrier cable is a fiber rope with a diameter of 16 mm, and a

total length of 670 m. Eight hanging nets are suspended on the carrier cable. The wire is fixed with a spherical joint at its left side and released freely at the other side. The material parameters of the ropes are listed in Table 1. The simulation program for this model was developed and executed in the MATLAB 2023b software environment. The duration of the dynamic simulation is 5 s. Result visualization was implemented based on ParaView 5.4.1. This is an open-source post-processing visualization engine. It can generate the result configuration by outputting a 'vtk' format result file through the simulation program and render the cloud map using the color data. It is also possible to generate animations by continuously drawing multiple frames of images [34].

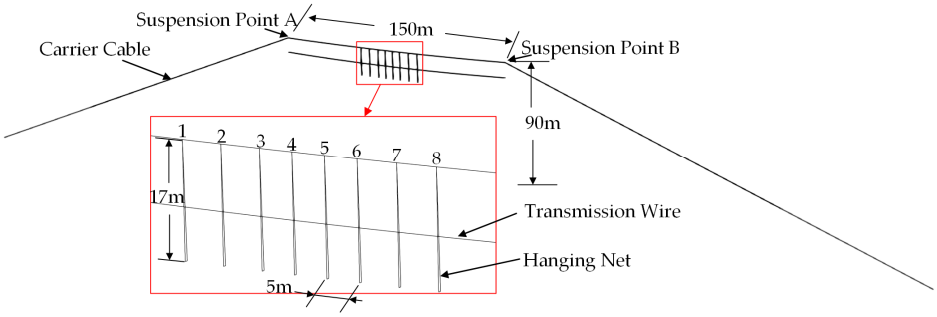


Figure 7. Hanging net shielding system with suspension ropes.

Table 1. Material parameters.

	Length (m)	Diameter (mm)	Density (kg/m^3)	Linear Density (kg/m)	Elastic Modulus (GPa)
Wire	155	26.8	2376	1.35	79
Carrier Cable	670	16	870	0.13	63
Sling Cable	17	8	870	0.04	63

Figure 8 shows the configuration of the wire and the shielding system at different instants with a tension distribution cloud map. The maximum tension appears at the connection point between the carrier cable and the rightmost hanging net. This net is also the one subjected to the most severe force among the eight hanging nets. The changing history of the tension at this point is presented in Figure 9. Figure 10 gives the changing of tension in the hanging net which suffers largest tension among the eight hanging nets. Figure 11 shows the tension in the carrier cable at the two suspension positions A and B.

From the continuous change process of the configuration of the wire and the hanging net shielding system shown in Figure 8, it can be observed that after breaking, the wire falls on the horizontal pulley. Under the action of impact loads, the slings of the hanging net experience severe transverse vibration and shaking, and the carrier cable also undergoes significant downward deflection and deformation due to the pulling of the hanging nets. The hanging net fully restrains and supports the wire, therefore protects the facilities under it. After the wire is in full contact with each hanging net, its free section still swings rapidly under the action of gravity, thus bringing a second tension peak to the carrier cable and the hanging net. This figure provides a comprehensive overview of the entire shielding system during the dynamic process, which can be used to assess the rationality of the results and offer an explanation for the tension outcomes. From Figure 9 one can find that the maximum tension in of the carrier cable throughout the entire process is 110 kN. The maximum tension of the fiber rope with a diameter of 16 mm is 210 kN, so the carrier cable has a safety margin of 1.9 times. Similarly, it can be observed from Figure 10 that the peak value of the tension in the hanging net is 9 kN, while the maximum tension of the fiber rope with a diameter of 8 mm is 60 kN. It indicates that the hanging net has a safety margin of

6.7 times. The tension results can effectively guide the design since in engineering design it is necessary to select fibers with smaller diameters as much as possible while ensuring safety in order to reduce the system's weight, lower the construction difficulty and control the construction cost. The tension in the carrier cable at the two suspension points given in Figure 11 is important as it is of great significance for verifying the structural safety of the iron tower. The results presented above demonstrate the effectiveness of the proposed modeling and computational methods.

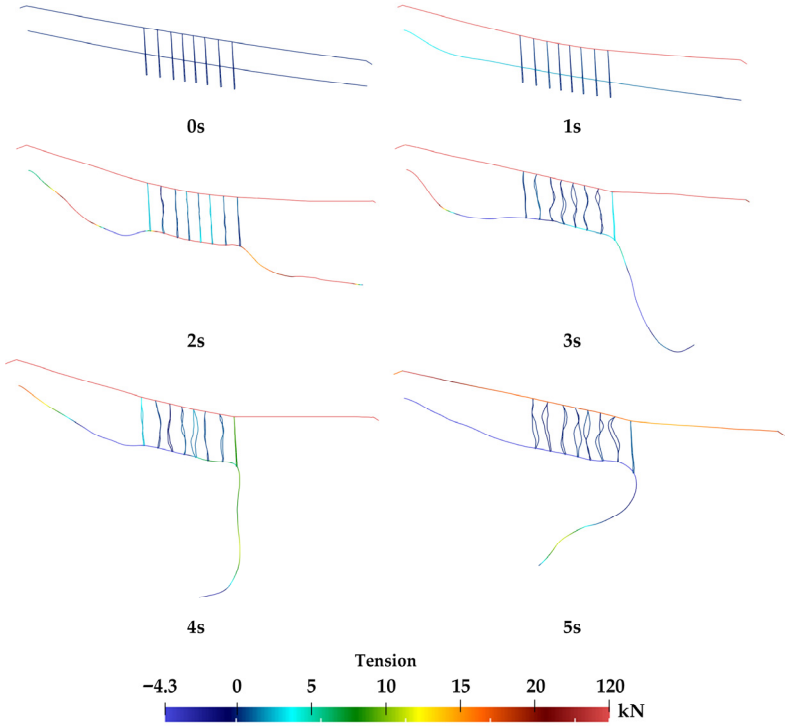


Figure 8. Configurations of the wire and barrier net at different time instants.

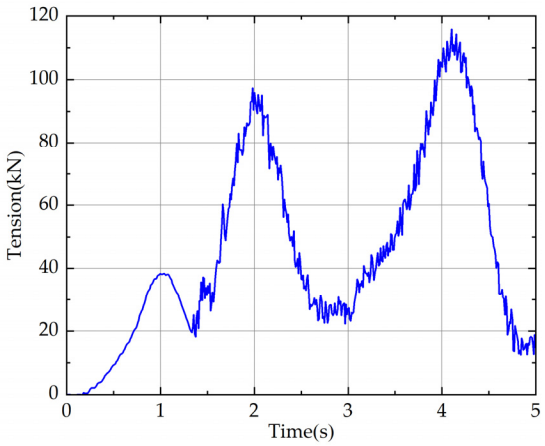


Figure 9. Tension in the carrier cable at the net connection points.

Figures 12 and 13 show the configuration of hanging nets 4 and 5 at different instants with a tension distribution cloud map. Figure 14 presents the changing history of the tension in carrier cable at connection points with hanging nets 4 and 5. Figure 15 shows the contact force at two suspension points between the carrier cable and the pulley of positions A and B.

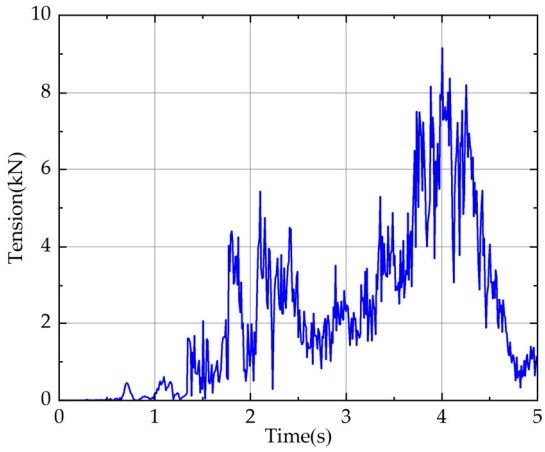


Figure 10. Tension variation in the hanging net which is subjected to the most severe force.

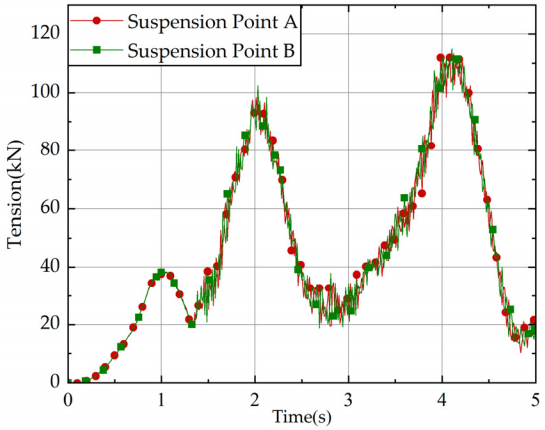


Figure 11. Tensions in the carrier cable at two suspension points.

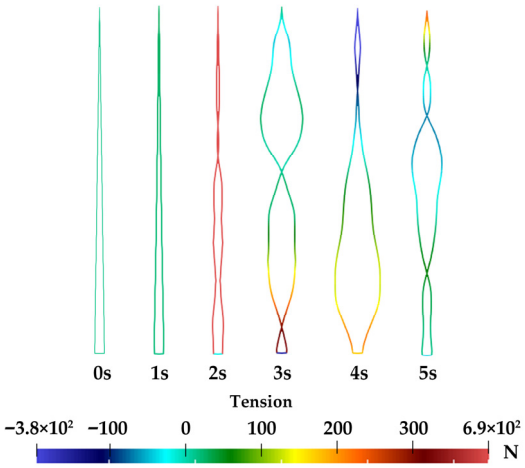


Figure 12. Configurations of hanging net 4 at different time instants.

Figures 12 and 13 provide overviews of the two hanging nets during entire impact process. With the impact of the wire, the hanging net will undergo large-scale motion and large deformation coupling, presenting severe shaking. This modeling method can effectively capture the dynamic response process. Although the hanging net has significant deformation, it can still provide good protection. Figure 14 gives the variation in the tension in carrier cable at the other positions. The two peaks of the tension in the carrier cable can also be observed. It indicates that during the design process, damping and energy absorption devices can be used in series within the carrier cable to quickly mitigate the

oscillations caused by the impact from the transmission wire. The peak contact force between the two suspension points of the carrier cable and the pulley is 40 kN, which is much lower than the maximum stress of the carrier cable. The results presented in Figure 15 are of great significance for the selection of pulleys and structural safety.

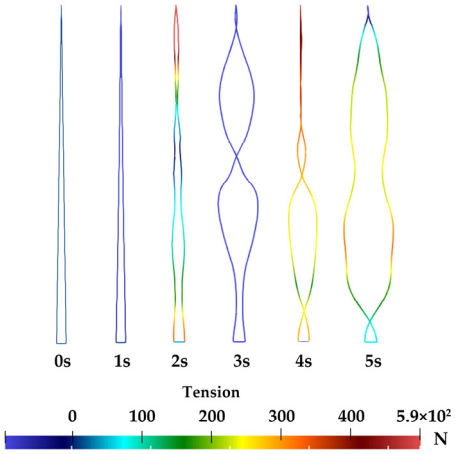


Figure 13. Configurations of hanging net 5 at different time instants.

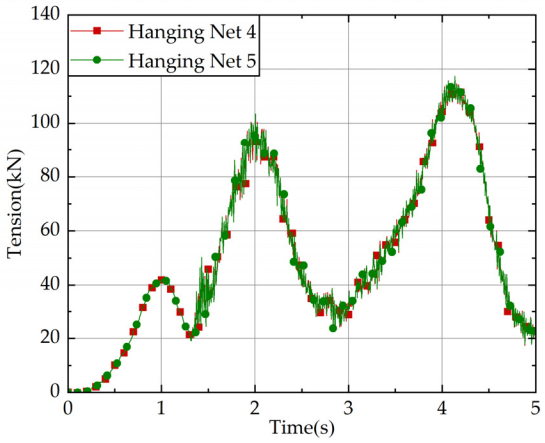


Figure 14. Tension in the carrier cable at connection points with hanging net 4 and 5.

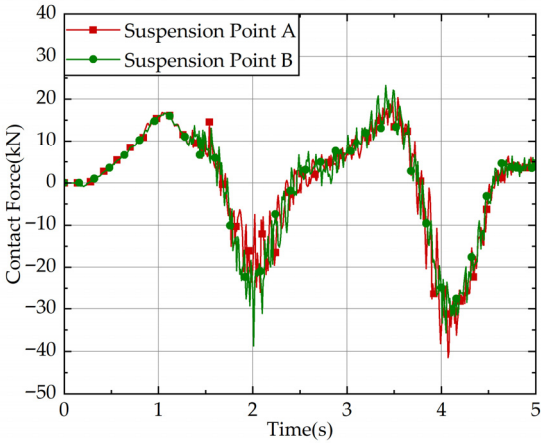


Figure 15. The contact force at two suspension points between the carrier cable and the pulley.

As summary, important results are given in Table 2, which could serve as a reference for the selection of fiber ropes. For instance, in power construction, it is usually required that the safety factor of the fiber rope should not be lower than two. If the rope gets wet by

rain, the maximum bearing tension will decrease to 70% of its value when it is dry. When running this simulation program, the working conditions can be simulated by increasing the yarn density, thereby providing a reference for the strength verification during the design process. Furthermore, the contact force exerted by the suspension cable on the pulley is an important load in the safety calculation of the tower structure. It has a significant impact on the strength and stability of the steel structure. Therefore, the simulation results need to be as accurate as possible.

Table 2. Summary results.

	Diameter (mm)	Largest Value (kN)	Maximum Tension Allowed (kN)	Safety Margin
Carrier Cable Tension	16	110	210	1.9
Sling Cable Tension	8	9	60	6.7
Contact Force to Pulley A		−41		
Contact Force to Pulley B		−35		

6. Conclusions

In this research, a multibody system dynamics analysis model for the hanging net shielding system was established using the ANCF cable element. The element kinematic description and elastic force expression are presented. The initial configuration of the carrier cable is calculated according to the initial tension through the catenary line formulation. Based on the assumption of a single continuous contact region and building upon a spatial beam–beam contact model, a contact search algorithm between the sling's horizontal pulley and the wire was developed. The algorithm treats the wire as an independent continuous spatial curve, uses Newton iteration to find the closest points between the pulley and the wire, and if contact occurs, employs a bisection method to search bilaterally until the contact region boundaries are identified. Finally, contact forces, defined in integral form, are applied based on the penalty method. A full-scale hanging net shielding system was established to verify the proposed modeling and dynamic analysis method. The results show that the carrier cable and sling cable endured two peak impacts within a period of 5 s. The first time was the initial contact of the wire, while the second time had a higher peak value, which originated from the downward swing of the free end after the wire was fully in contact. The largest tension in the carrier cable is 110 kN, while the maximum tension of the fiber rope with a diameter of 16 mm is 210 kN, so the carrier cable has a safety margin of 1.9 times. The largest tension in the sling cable is 9 kN, while the maximum tension of the fiber rope with a diameter of 8 mm is 60 kN, which indicates that the safety margin is 6.7 times. The results obtained through proposed dynamic analysis procedure can help the engineers to employ a more economical and reasonable configuration of the hanging net and the diameter of the fiber rope, and also shorten the design cycle, save design and construction costs, and ensure the safety of power construction. Further research can be conducted on the following two aspects. Firstly, the parameterization of the modeling method proposed in this paper can be carried out, thereby enabling the rapid modeling of the complex hanging net shielding system, and improving the efficiency of engineering design. Secondly, experiments can be conducted to verify the correctness of the algorithm proposed in this paper.

Author Contributions: Conceptualization, Q.L.; methodology, Q.L.; software, X.Z.; validation, X.Z.; formal analysis, Q.Z.; investigation, Q.Z.; resources, Q.L.; data curation, Q.L.; writing—original draft, Y.B.; visualization, Y.B.; supervision, Z.Y.; project administration, Z.Y.; writing—review and editing, Z.Y. All authors have read and agreed to the published version of the manuscript.

Funding: This research was funded by the Science and Technology Project of State Grid Jiangsu Electric Power Co., Ltd, grant number J2024032.

Data Availability Statement: The raw data supporting the conclusions of this article will be made available by the authors on request.

Conflicts of Interest: Authors (Qiang Liu, Xi Zheng and Qiuhan Zhang) were employed by the company Xuzhou Power Transmission & Transformation Co., Ltd. The remaining authors declare that the research was conducted in the absence of any commercial or financial relationships that could be construed as a potential conflict of interest.

Nomenclature

$\mathbf{S}$	The shape function of element, unitless.
S_1, S_2, S_3, S_4	The components of the shape function, unitless.
$\mathbf{I}_{3\times3}$	The 3×3 identity matrix, unitless.
ξ	The dimensionless material coordinate, unitless.
l	The length of element, m.
$\mathbf{M}^{\mathrm{e}}$	The mass matrix of element, kg.
ρ	The reference density, kg/m^3.
V	The volume of element, m^3.
U	The strain energy, J.
A	The cross-section area of element, m^2.
E	The modulus of elasticity, Pa.
I	The second moment of the cross-section, m^4.
ε_{xx}	The strain along the axis, unitless.
κ	The spatial measurement of curvature, 1/m.
r_x	The first derivative with respect to the material coordinates, m.
r_{xx}	The second derivative with respect to the material coordinates, 1/m.
$\mathbf{e}$	The nodal coordinate vector of element, m.
$\mathbf{Q}_{\mathrm{e}}$	The generalized elastic force of the element, N.
$\mathbf{Q}_{\mathrm{s}}$, $\mathbf{Q}_{\kappa}$	The generalized elastic forces related to axial stretching and bending, N.
e_i	The i-th component of the nodal coordinate vector, unitless.
$\mathbf{S}_x$	The derivative of the element shape function with respect to the material coordinate, unitless.
$\mathbf{S}_{x,i}$, $\mathbf{S}_{xx,i}$	The i-th column of the first and second derivative of element shape function, unitless.
f, g	The intermediate functions in the formulation of the curvature, f has the unit of 1/m, g is unitless.
f_x	The arc sag value at an arbitrary point on the cable, m.
T	The composed initial tension on the carrier cable, N.
w	The linear density of carrier cable, N/m.
L	The span between the two transmission towers, m.
L_A	The horizontal distance from the lowest point O of the overhead line to suspension point A, m.
h	The vertical height difference between the two suspension points, m.
$\mathbf{f}$	The contact force at this Gauss point, N.
$\mathbf{V}_{\mathrm{n}}$	The normal vector, unitless.
$\mathbf{V}_{\mathrm{t}}$	The tangential vector, unitless.
f_{n}	The normal contact force at this Gauss point, N.
f_{t}	The tangential contact force at this Gauss point, N.
δ	The penetration depth, m.
$\dot{\delta}$	The penetration velocity, m/s.
k	The contact stiffness coefficient, N/m.
c	The contact damping coefficient, N·s/m.

μ	The dynamic friction coefficient, unitless.
n_c	The number of Gauss points, unitless.
w_{k}	The Gauss integration weight coefficient, unitless.
$\mathbf{S}_k$	The shape function of the cable element currently in contact, unitless.
$\mathbf{Q}_{\mathrm{c}}$	The generalized contact force, N.
$\mathbf{r}^{P_1}$, $\mathbf{r}^{P_2}$, $\mathbf{r}^{P_3}$, $\mathbf{r}^{Q_1}$, $\mathbf{r}^{Q_2}$, $\mathbf{r}^{R_1}$, $\mathbf{r}^{R_2}$	The global position vectors of point $\mathbf{P}_1$, $\mathbf{P}_2$, $\mathbf{P}_3$, $\mathbf{Q}_1$, $\mathbf{Q}_2$, $\mathbf{R}_1$, $\mathbf{R}_2$, m.
$\ddot{\mathbf{e}}$	The generalized acceleration of element nodal coordinate, m/s^2.
$\boldsymbol{\lambda}$	The Lagrange multiplier, N.
$\mathbf{C}$	The system constraint equations, unitless.
$\mathbf{C}_e$	The Jacobian matrix of constraint equation with respect to generalized coordinates, unitless.
t	The time, s.

References

1. Barbieri, N.; de Souza Junior, O.H.; Barbieri, R. Dynamical analysis of transmission line cables. Part 2—Damping estimation. *Mech. Syst. Signal Process.* **2004**, *18*, 671–681. [CrossRef]
2. Barbieri, N.; de Souza Junior, O.H.; Barbieri, R. Dynamical analysis of transmission line cables. Part 1—Linear theory. *Mech. Syst. Signal Process.* **2004**, *18*, 659–669. [CrossRef]
3. Xu, F.; Li, D.; Gao, P.; Zang, W.; Duan, Z.; Ou, J. Numerical simulation of two-dimensional transmission line icing and analysis of factors that influence icing. *J. Fluids Struct.* **2023**, *118*, 103858. [CrossRef]
4. Yang, L.; Chen, Y.; Mei, L.; Hao, Y.; Li, L.; Huang, H.; Zhang, Y.; Zhang, L.; Yang, L. Prediction method for response characteristics parameters of isolated-span overhead lines after ice-shedding based on finite element simulation and machine learning. *Electr. Power Syst. Res.* **2024**, *229*, 110141. [CrossRef]
5. Wen, N.; Yan, B.; Mou, Z.; Huang, G.; Yang, H.; Lv, X. Prediction models for dynamic response parameters of transmission lines after ice-shedding based on machine learning method. *Electr. Power Syst. Res.* **2022**, *202*, 107580. [CrossRef]
6. Gao, M.; Chen, Z.; Su, J.; Su, N.; Liu, C.; Zhang, J.; Chen, H. Experimental study on the galloping characteristics of single ice-coated transmission lines under oblique flows. *Sci. Rep.* **2023**, *13*, 5172. [CrossRef]
7. Zhao, G.; Lu, Z.; Wang, X.; Peng, Y.; Chang, S. Full Scale Experiment for Vibration Analysis of Ice-Coated Bundled-Conductor Transmission Lines. *KSCE J. Civ. Eng.* **2022**, *26*, 336–352. [CrossRef]
8. Qin, Q.; Tu, X.; Hu, Y.; Wang, Z.; Yu, L.; Hou, S. Modeling and Loading Effect of Wind on Long-Span Cross-Rope Suspended Overhead Line with Suspension Insulator. *Buildings* **2024**, *14*, 656. [CrossRef]
9. Sørum, S.H.; Fonseca, N.; Kent, M.; Faria, R.P. Modelling of Synthetic Fibre Rope Mooring for Floating Offshore Wind Turbines. *J. Mar. Sci. Eng.* **2023**, *11*, 193. [CrossRef]
10. Hong, A.; Jia, M.; Wang, M.; Niu, D.; Zhao, W. Research on Damage Mechanism of Towed Wire Rope on Dynamic Simulation and Finite Element Modeling. In Proceedings of the 37th Chinese Control and Decision Conference, CCDC, Xiamen, China, 16–19 May 2025; pp. 3865–3870. [CrossRef]
11. Kang, Z.; Sui, H.; Ai, S.; Zhang, Y. Study on the Calculation Method for the Dynamic Behavior of Polyester Rope. *J. Mar. Sci. Appl.* **2024**, *23*, 398–405. [CrossRef]
12. Cheng, X.; Cai, Y. Dynamic Characteristics Modeling for Electric Transmission Line Tower System Using the Free Interface Modal Synthesis. In *Proceeding of the 9th International Symposium on Lifeline and Infrastructure Earthquake Engineering*; Lecture Notes in Civil Engineering; Springer Nature: Singapore, 2025; Volume 721, pp. 547–557. [CrossRef]
13. KC, P.; Naghibolhosseini, M.; Zayernouri, M. Multiphysics Modeling of Power Transmission Line Failures Across Four US States. *Modelling* **2024**, *5*, 1745–1772. [CrossRef]
14. Deng, L.; Xia, Y.; Chen, X.; Ouyang, B.; Lu, L.; Zhang, C.; Zhang, X.; Xiong, Y. Dynamic Research on Steel Wire Rope Rigging Under Impact Bending Wave Load. *Modelling* **2025**, *6*, 142. [CrossRef]
15. Gu, Y.; Lan, P.; Cui, Y.; Li, K.; Yu, Z. Dynamic interaction between the transmission wire and cross-frame. *Mech. Mach. Theory* **2021**, *155*, 104068. [CrossRef]
16. Gu, Y.; Gu, Z.; Yu, Z.; Lan, P.; Lu, N. Dynamic analysis of the flexible protection system for electricity transmission engineering. *Mech. Sci.* **2025**, *16*, 75–86. [CrossRef]
17. Xia, Y.; Shi, Q.; Ma, Y.; Ni, H. Dynamic modeling and simulation of high-voltage wire impacting flexible protection system. In Proceedings of the 2025 International Conference on Software Engineering and Computer Applications, SECA, Kunming, China, 13–15 June 2025; pp. 148–155. [CrossRef]

18. Shabana, A.A. An overview of the ANCF approach, justifications for its use, implementation issues, and future research directions. *Multibody Syst. Dyn.* **2023**, *58*, 433–477. [CrossRef]
19. Gerstmayr, J.; Irschik, H. On the correct representation of bending and axial deformation in the absolute nodal coordinate formulation with an elastic line approach. *J. Sound Vib.* **2008**, *318*, 461–487. [CrossRef]
20. Wang, Q.; Tian, Q.; Hu, H. Dynamic simulation of frictional contacts of thin beams during large overall motions via absolute nodal coordinate formulation. *Nonlinear Dyn.* **2014**, *77*, 1411–1425. [CrossRef]
21. Wang, Q.; Tian, Q.; Hu, H. Dynamic simulation of frictional multi-zone contacts of thin beams. *Nonlinear Dyn.* **2015**, *83*, 1919–1937. [CrossRef]
22. Escalona, J.L.; Sugiyama, H.; Shabana, A.A. Modelling of structural flexiblity in multibody railroad vehicle systems. *Veh. Syst. Dyn.* **2013**, *51*, 1027–1058. [CrossRef]
23. Pappalardo, C.M.; De Simone, M.C.; Guida, D. Multibody modeling and nonlinear control of the pantograph/catenary system. *Arch. Appl. Mech.* **2019**, *89*, 1589–1626. [CrossRef]
24. Peng, C.; Yang, C.; Xue, J.; Gong, Y.; Zhang, W. An adaptive variable-length cable element method for form-finding analysis of railway catenaries in an absolute nodal coordinate formulation. *Eur. J. Mech. A/Solids* **2022**, *93*, 104545. [CrossRef]
25. Luo, S.; Fan, Y.; Cui, N. Application of Absolute Nodal Coordinate Formulation in Calculation of Space Elevator System. *Appl. Sci.* **2021**, *11*, 1576. [CrossRef]
26. Takayama, S.; Takehara, S.; Yuasa, R. Contact Analysis of Mobility Devices Based on Tension. *Modelling* **2021**, *2*, 370–384. [CrossRef]
27. Zhang, Y.; Guo, J.W.; Liu, Y.Q.; Wei, C. Absolute Nodal Coordinate Formulation-Based Decoupled-Stranded Model for Flexible Cables With Large Deformation. *J. Comput. Nonlinear Dyn.* **2021**, *16*, 031005. [CrossRef]
28. Zhang, P.; Duan, M.; Gao, Q.; Ma, J.; Wang, J.; Saevik, S. Efficiency improvement on the ANCF cable element by using the dot product form of curvature. *Appl. Math. Model.* **2022**, *102*, 435–452. [CrossRef]
29. Wang, J.; Yang, Q.; Huang, B.; Ouyang, Y. Adaptive ANCF method described by arbitrary Lagrange-Euler formulation with application in variable-length underwater tethered systems moving in limited spaces. *Ocean Eng.* **2024**, *297*, 117059. [CrossRef]
30. Escalona, J.L.; Mohammadi, N. Advances in the modeling and dynamic simulation of reeving systems using the arbitrary Lagrangian–Eulerian modal method. *Nonlinear Dyn.* **2022**, *108*, 3985–4003. [CrossRef]
31. Li, K.; Liu, M.L.; Yu, Z.Q.; Lan, P.; Lu, N.L. Multibody system dynamic analysis and payload swing control of tower crane. *Proc. Inst. Mech. Eng. Part K J. Multi-Body Dyn.* **2022**, *236*, 407–421. [CrossRef]
32. Han, Y.; Ma, X.; Zhang, J.; Shi, X. Investigation of Rope-sheave Dynamic Contact Characteristics Based on Absolute Nodal Coordinate Formulation. *J. Phys. Conf. Ser.* **2025**, *3004*, 012054. [CrossRef]
33. *DL/T 5301-2013*; Construction Technology Guide for Tension Stringing of Overhead Transmission Line When Over-Crossing Live Lines Without Cross Frame. National Energy Administration of China: Beijing, China, 2013.
34. ParaView. Open-Source, Multi-Platform Data Analysis and Visualization Application. Available online: https://www.paraview.org (accessed on 14 January 2026).

Disclaimer/Publisher's Note: The statements, opinions and data contained in all publications are solely those of the individual author(s) and contributor(s) and not of MDPI and/or the editor(s). MDPI and/or the editor(s) disclaim responsibility for any injury to people or property resulting from any ideas, methods, instructions or products referred to in the content.